PAPER

Check for updates

Composition-tuned MAPbBr₃ nanoparticles with addition of Cs⁺ cations for improved photoluminescence†

Sai S. H. Dintakurti, [ID] *[abc] Parth Vashishtha, [ID] [b] David Giovanni, [ID] [d] Yanan Fang, [ID] [b] Norton Foo, [ID] [b] Zexiang Shen, [ID] [ade] Claude Guet, [ID] [ab] Tze Chien Sum [ID] [d] and Tim White*[b]

Hybrid organic–inorganic lead halide perovskite nanoparticles are promising candidates for optoelectronic applications. This investigation describes the structural and optical properties of $MA_xCs_{1-x}PbBr_3$ mixed cation colloidal nanoparticles spanning the complete compositional range of Cs substitution. A monotonic progression in the cubic lattice parameter (*a*) with changes in the Cs⁺ content confirmed the formation of mixed cation materials. More importantly, time-resolved photoluminescence (TRPL) revealed the optimized 13 mol% Cs nanoparticle composition exhibits the longest charge carrier lifetime and enhancement in radiative pathways. This sample also showed the highest photoluminescence quantum yield (PLQY) of ~88% and displays ~100% improvement in the PLQY of pure MAPbBr₃ and CsPbBr₃. Prototype LEDs fabricated from $MA_{0.87}Cs_{0.13}PbBr_3$ were demonstrated.

Introduction

Hybrid organic–inorganic lead halide perovskites (LHPs) have been widely explored for optoelectronic applications resulting in solar cells with a record power conversion efficiency (PCE) of 25.5% and light emitting diodes with an external quantum efficiency (EQE) exceeding 20%.[1–7] The key advantages of this class of materials are solution processability, inexpensive starting materials, composition tunable band gap, high hole and electron mobility, and high defect tolerance.[8,9] Despite showing high efficiency, prototype perovskite materials such as MAPbX₃ and FAPbX₃ (where MA = methylammonium; FA = formamidinium; X = Br, I) suffer from phase instability, poor reproducibility, and thermal instability.[10–12] Saidaminov et al.[13] found lattice strain in perovskite induces point defects leading to structural degradation and PLQY quenching. Lattice perfection can be improved by the addition of inorganic Cs⁺ that improves phase stability by strain relaxation leading to more reproducible optoelectronic devices with improved thermal

stability.[14,15] A similar strategy of strain relaxation in FAPbI₃ produced solar cells with PCE of 24.4%.[16] In contrast, compressive strain in CsPbBr₃ has been also found to be detrimental towards stability.[17] On the other hand, Zhang et al.[18] reported significant improvement in thin-film LEDs using mixed cation $Cs_{0.87}MA_{0.13}PbBr_3$ material when compared to pure CsPbBr₃. In general, it is likely that strain relaxation can be achieved by incorporating additional cations in the ABX₃ LHPs, to improve structural stability and optoelectronic properties.

Following the synthesis of mixed-cation perovskite powders and appreciable crystals, research focused on analogous nanoparticles to exploit their high PLQY, quantum confinement, narrow emission linewidth, and size-tuneable optical properties.[19–21] These studies were motivated, in part, because perovskite nanoparticle LEDs show comparable performance to state-of-the-art CdSe based QDLEDs.[5,22,23] Song et al.[24] synthesised 15 mol% FA doped CsPbBr₃ ($Cs_{0.85}FA_{0.15}PbBr_3$) demonstrating 61% PLQY. Later, Vashishtha et al.[13,19] demonstrated the first triple cation synthesis of $Cs_x(MA_{0.17}FA_{0.83})_{1-x}PbBr_3$ ($x = 0$–0.15) for LED applications. These nanoparticles exhibit high phase stability and reproducibility confirming the expected advantages of mixed-cation perovskites. Premkumar et al. were the first to synthesize cesium–methylammonium mixed-cation lead bromide nanoparticles exhibiting twin PL emission peaks for Cs 20% and 40% compositions ($Cs_{1-x}MA_xPbBr_3$, $x = 0.2, 0.4$).[25] The twin emission was attributed to the bi-phase nature of the samples; although Cs-MA should show a continuous solid solution and be completely miscible according to perovskite tolerance factor considerations.[25,26] It was also observed that these Cs-MA based LHP nanoparticles were larger than ~12 nm

[a] ERI@N, Interdisciplinary Graduate School, Nanyang Technological University, Singapore 639798. E-mail: sriharsh001@e.ntu.edu.sg

[b] School of Materials Science and Engineering, Nanyang Technological University, Singapore 639798. E-mail: tjwhite@ntu.edu.sg

[c] Department of Physics, University of Warwick, Coventry, West Midlands, CV4 7AL, UK

[d] School of Physical and Mathematical Sciences, Nanyang Technological University, Singapore 639798

[e] Centre for Disruptive Photonic Technologies, CNRS International NTU Thales Research Alliance, Nanyang Technological University, Singapore 639798

† Electronic supplementary information (ESI) available. See DOI: 10.1039/d1ra03965b

with micaceous morphology that inhibits colloidal solubility/stability and reduces the advantages of strong quantum confinement.[25,27] As colloidal stability is essential to fabricate thin-film optoelectronic devices, the present work was prompted by the desire to synthesise single phase $MA_xCs_{1-x}PbBr_3$ colloidally stable nanoparticles.

Here, $MA_xCs_{1-x}PbBr_3$ ($x = 0-1$) homogeneous nanoparticles were synthesized using a facile room-temperature ligand-assisted reprecipitation (LARP) method facilitating precise linking of Cs content with the structural and optical properties.[19,28] Rietveld refinement of powder X-ray diffraction (XRD) patterns and X-ray photoelectron spectroscopy (XPS) monitored crystallochemical evolution were correlated with optical properties, including PL emission wavelength, charge carrier lifetime, and PLQY. Lastly, the optimized $MA_{0.87}Cs_{0.13}PbBr_3$ nanocrystals were fabricated as electrically-driven LEDs.

Synthesis

A homogenous substitution of Cs^+ ions in $MAPbBr_3$ requires overcoming the solubility differences between Cs and MA in the dimethylformamide (DMF) solvent. Following the strategy reported by Veldhuis *et al.*,[19,28] the cesium solubility in DMF was enhanced by using a complexing agent, dibenzo 21-crown-7 ether. A continuous solid solution series with the general composition $MA_xCs_{1-x}PbBr_3$ (where $x = 0$, 0.13, 0.25, 0.37, 0.5, 0.63, 0.75, 0.87, 1) was prepared with slight modification of the LARP method reported earlier where 0.4 mmol of the salts were dissolved in 2 mL of DMF to prepare the perovskite precursor solution (see Table S4†). 150 μL of this solution was added

dropwise into a solution containing toluene and ligand. The resulting nanoparticles were purified and dissolved in hexane for further processing (refer ESI† for details). This procedure was used across the entire compositional range.

Results and discussion

Structural properties

$CsPbBr_3$ exhibits temperature-dependent polymorphism, and appreciable crystals are orthorhombic (*Pnma*) at room temperature.[29] Unambiguous characterisation of $CsPbBr_3$ nanoparticles by laboratory powder X-ray diffraction can be challenging as the changes in lattice parameters, for example orthorhombic to cubic are small, and easily obscured by Scherrer broadening and preferred orientation, but can sometimes be discerned using transmission synchrotron methods.[30,31] $MAPbBr_3$ is cubic ($Pm\bar{3}m$) with dynamic methyl ammonium ions. It is reasonable then to adopt a cubic model to monitor lattice changes and the compositional progression from $MAPbBr_3$ to $CsPbBr_3$.

X-ray photoelectron spectroscopy (XPS) provided an independent verification of composition, and while XPS is surface sensitive, photoelectrons can escape from the centre of quantum dots/nanoparticles and the extracted compositions are representative of the perovskite chemistry.[32,33] XPS examined the binding energies of the Cs 4d (74–78 eV) and Br 3d (64–71 eV) emissions (Fig. 1a and S3†), and as the intensity of Cs peaks reduces monotonically with increasing Br content, the integrated doublet peak areas were corrected for sensitivity to
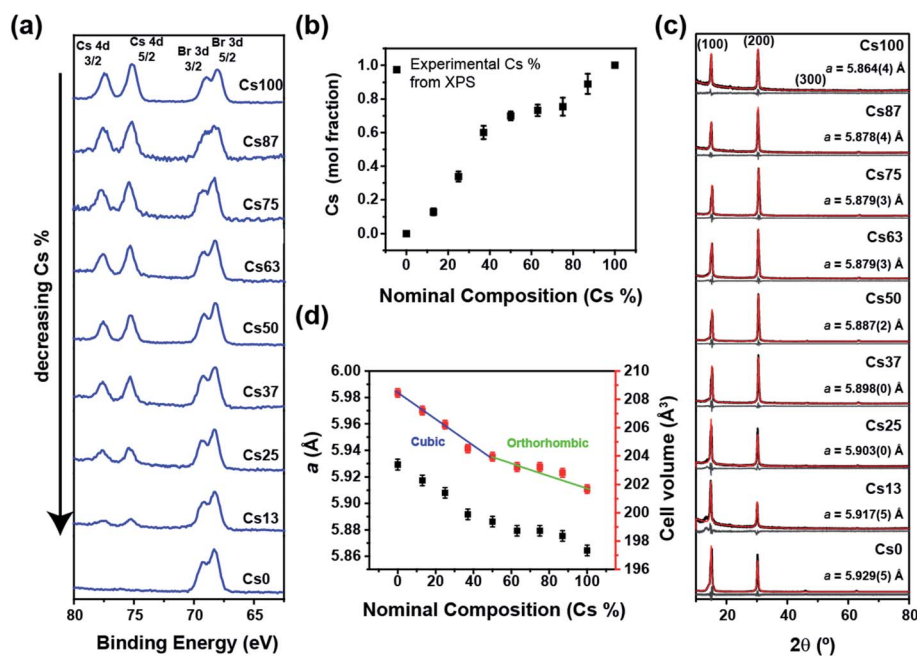

Fig. 1 (a) X-ray photoelectron spectroscopy (XPS) data of the prepared nanoparticle samples of the solid solution series $MA_xCs_{1-x}PbBr_3$. (b) A plot of Cs content obtained from elemental composition analysis of XPS data. (c) Powder X-ray diffraction patterns of drop casted nanoparticle samples on Si zero background crystals. The experimental (black line), calculated (red line) and difference (grey line) curves from Rietveld refinement using a cubic model. Strong preferred orientation is observed along (1 0 0) direction. (d) Evolution of lattice parameter a and unit cell volume obtained from Rietveld refinement of powder X-ray diffraction pattern in the solid solution series $MA_xCs_{1-x}PbBr_3$.

obtain atomic ratios. As Pb^{2+} stoichiometrically occupies the B-site, the Pb 4f and Cs 4d peak ratio were used to confirm the putative Cs content (Fig. 1a, b, S3 and Table S3†) and shows a slight enrichment between the nominal compositions 25 to 63% Cs. This likely arises from a systematic error in the synthesis or composition measurement rather than a miscibility gap.

The powder X-ray diffraction (XRD) patterns of drop cast samples exhibit (100) reflections characteristic of cubic MAPbBr$_3$ (space group $Pm\bar{3}m$) (Fig. 1c) that was used for Rietveld refinement.[34] The XRD peaks were Scherrer broadened[18,35] as expected from nano-sized crystallites. Compared to Cs^+ the MA^+ ion scatters X-rays more weakly and has a larger effective ionic radius leading to a progressive decrease in the (200)/(100) peak intensity ratio with decreasing cesium content in MA_x-$Cs_{1-x}PbBr_3$ (Fig. 1c) while the refined lattice parameter reduces monotonically with a slight deviation around 50% (Fig. 1d), in agreement with the higher cesium content observed from XPS. Furthermore, the cell volume (Fig. 1d and Table S1†) shows an inflection that may be attributed to a reduction symmetry to orthorhombic ($Pbnm$) as in CsPbBr$_3$. Such compositional dimorphism could not be confirmed due to strong textural effects and crystal size broadening. Overall, XRD and XPS confirm the systematic homogenous evolution of mixed-cation structure with cesium incorporation.

Transmission electron microscopy found the MA-rich compositions displayed spherical morphology while the Cs rich compositions show cuboid particles pointing to different surface energies of the nanoparticles, however further investigation of the surface interactions is required. An average shifted histogram was constructed to estimate particle sizes of 4.6 ± 1.3 and 13.5 ± 2.9 nm for 25 mol% Cs and 75 mol% Cs samples, respectively (Fig. 2 and S1†). A gradual increase in particle size from 3.5 to 18.5 nm was observed in passing from MA to Cs rich compositions. As the solubility of the Cs ions in DMF/toluene is lower than MA ions, the rate of precipitation is correspondingly faster for Cs rich precursors, and as a standard reaction time of 5 min was used for all the samples, this accounts for the increasing particle size towards the Cs endmember.

Cesium-rich were less susceptible to degradation during electron beam irradiation enabling the collection of higher magnification bright-field images with lattices where 2.9 Å and 5.7 Å fringes correspond to the (200) and (100) planes of cubic perovskite (Fig. 2).

Photophysical properties

Cs^+ incorporation in MAPbBr$_3$ results in a blue shift of absorption edge as well as the PL emission peak moving from
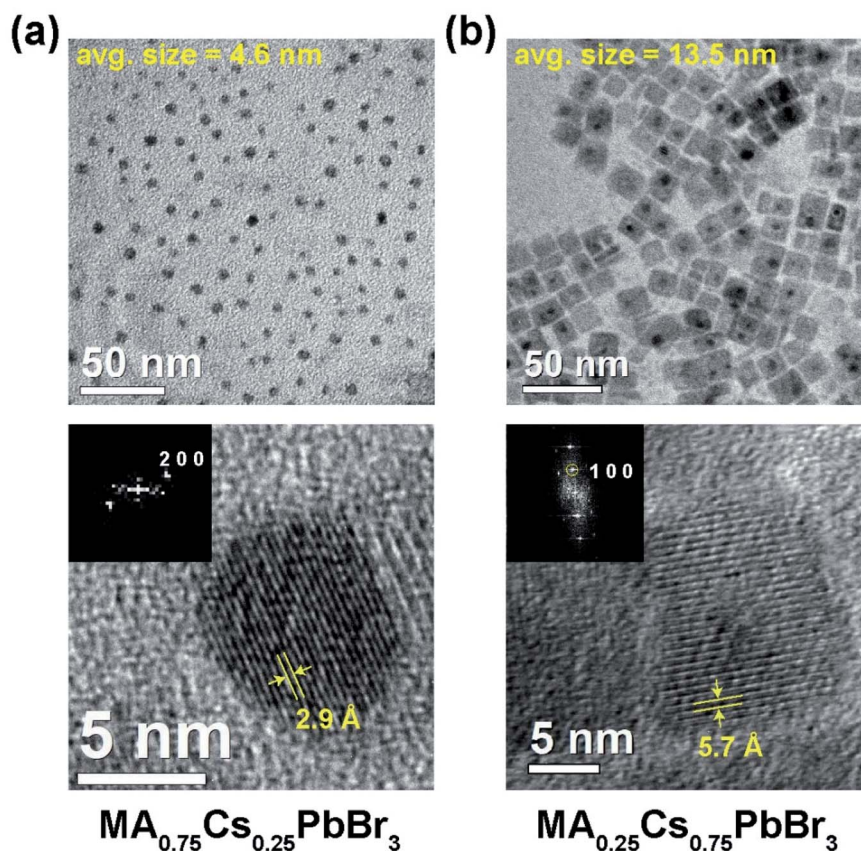

Fig. 2 Transmission electron micrographs of (a) 25 mol% Cs and (b) 75 mol% Cs samples showing spherical and cuboid particles of 5–14 nm size. The high magnification images (bottom) show lattice fringes with *d* spacings of 2.9 Å and 5.7 Å for 25 mol% Cs and 75 mol% Cs samples, respectively.
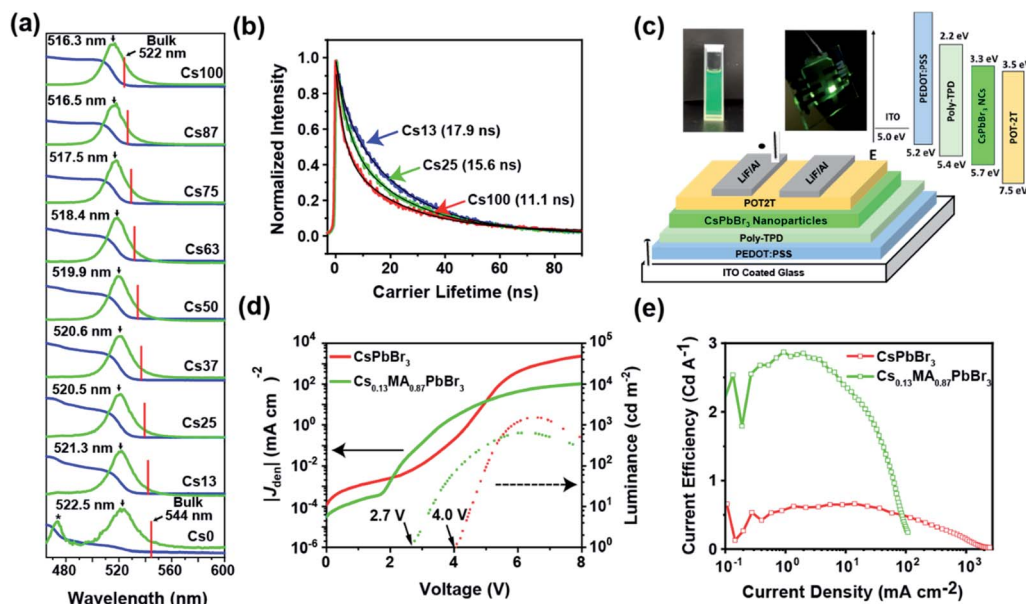
Fig. 3 (a) UV-vis absorption spectra (blue) and PL emission spectra (green) across the solid solution series $MA_xCs_{1-x}PbBr_3$. The bulk phase PL emission of end members is marked in red lines that are linearly interpolated for intermediate compositions (* indicates an impurity). (b) Time resolved photoluminescence (TRPL) data along with fitted curve (black line) showing 13 mol% Cs yielding the longest charge carrier lifetime. (c) Photograph of nanoparticles, LED device, architecture and band diagram of the active layer along with the hole and electron transporting layers, (d) current density–voltage–luminance (JV and LV) curves of $MA_{0.87}Cs_{0.13}PbBr_3$ and $CsPbBr_3$ LEDs, and (e) current efficiency vs. current density curve of $MA_{0.87}Cs_{0.13}PbBr_3$ and $CsPbBr_3$ LEDs.

522 nm for 0 mol% Cs sample to 516 nm for 100 mol% Cs sample (Fig. 3a), consistent with previous reports of pure $MAPbBr_3$ and $CsPbBr_3$ nanoparticles.[19,36,37] The bulk PL emission was estimated by linearly interpolating the PL emission peak from reported $CsPbBr_3$ and $MAPbBr_3$ data. This enables a deconvolution of size and composition effects. This blue shift in favour with contraction of lattice parameter by Cs^+ incorporation, further verifies a homogenous distribution of Cs^+ on the A site.[25,26] Moreover, all of these PL peaks exhibit FWHM smaller than 22 nm ensuring the monodispersity in the nanoparticles (Fig. 3a) and suitability for utilization in display devices. Pure $MAPbBr_3$ also shows the presence of a blue emission peak at 475 nm that has been previously observed in pure $MAPbBr_3$ and $FAPbBr_3$ nanoparticles and assigned to a 2D impurity phase

forming with the octylamine ligand[38,39] whose formation could be attributed to the low growth rate of nanoparticles during LARP synthesis. Reducing the ligand concentration may remove this fraction but results in larger particles. Moreover, the synthesis procedure used consistent experimental conditions across all samples to maintain a comparable size range, so further optimization on $MAPbBr_3$ nanoparticles was not performed.

To further investigate the optical properties, time resolved photoluminescence spectroscopy (TRPL) was conducted on the colloidal solution of as synthesized samples and analyzed using a bi-exponential decay fit (Tables 1, S2† and Fig. 3b). The 100 mol% Cs sample showed an exciton lifetime of 11 ns, which is consistent with a previous report of $CsPbBr_3$ nanoparticles

Table 1 PL emission, average particle size estimated from TEM, quantum yield and charge carrier lifetime data of nanoparticle samples from the solid solution series $MA_xCs_{1-x}PbBr_3$. The Bulk PL emission values of intermediate compositions are linearly interpolated from the reported single crystal PL emission of $CsPbBr_3$ and $MAPbBr_3$.* includes contribution from 2d impurity phase

Sample composition	Bulk PL emission (nm)	Nanoparticle PL emission (nm)	Nanoparticle PL fwhm (nm)	Crystallite size (TEM) (nm)	PLQY (%)	Carrier lifetime (±0.5 ns)	Bandgap (eV) (±0.1 eV)
Cs100	522.0 (ref. 27 and 37)	516.3	19.5	18.5 ± 3.5	48	11.1	2.37
Cs87	524.8	516.5	18.9	—	60	9.4	2.36
Cs75	527.5	517.5	18.8	13.5 ± 2.9	67	9.9	2.35
Cs63	530.3	518.4	19.7	—	76	9.7	2.34
Cs50	533.0	519.9	20.2	11.2 ± 2.6	74	15.6	2.33
Cs37	535.8	520.6	20.3	—	74	15.7	2.32
Cs25	538.5	520.5	21.2	4.6 ± 1.3	78	15.6	2.33
Cs13	**541.8**	**521.3**	**22.1**	—	**88**	**17.9**	**2.31**
Cs0	544.0 (ref. 37)	522.5	25.1	3.5 ± 0.9	42	25.5*	2.30

synthesized using a similar method.[40] By comparison, MAPbBr$_3$ nanoparticles exhibit an extremely long exciton lifetime of 25 ns due to the additional presence of blue-emitting species favoured by the formation of nanoplatelets, resulting in a downhill energy transfer process to the nanoparticles bandgap and the prolongation of population lifetime.[41] In contrast, mixed cation perovskites show a reverse trend in exciton lifetime such that increasing Cs$^+$ content reduces carrier lifetime from 17.9 ns for 13 mol% Cs to 9.4 ns for 87 mol% Cs sample (Table 1). In the current study, the major variables affecting the PLQY are particle size, defect number and composition. Orthorhombic (*Pbnm*) CsPbBr$_3$ nanoparticles reportedly have residual strain accommodated through octahedral tilting of the PbBr$_6$ octahedra[17,42,43] leading to higher defect concentrations and the degradation of photoluminescence properties.[13,17] As MAPbBr$_3$ is cubic (*Pm$\bar{3}$m*) without octahedral tilting, addition of methylammonium ions is expected to relax the lattice strain. The change in particle size is progressive, hence the increase in PLQY and subsequent decrease could be due to anomalous changes in strain affecting the number of structural defects. A future study will seek to quantitatively correlate quantifying strain and defect population.

The reduction in the exciton lifetimes and PLQY indicates the enhancement of a non-radiative channel that is undesirable for PL efficiency.[44] To investigate this effect, PLQY was measured in the colloidal solutions and found the 13 mol% Cs (MA$_{0.87}$Cs$_{0.13}$PbBr$_3$) shows the highest PLQY (~88%) with increased radiative recombination pathways (Table 1) compared to CsPbBr$_3$ (48%) and MAPbBr$_3$ (~42%). MA$_{0.75}$Cs$_{0.25}$PbBr$_3$ (78%) and MA$_{0.63}$Cs$_{0.37}$PbBr$_3$ (74%) also show good PLQY performance attributable to lattice strain relaxation.[13]

The excellent properties of MA$_{0.87}$Cs$_{0.13}$PbBr$_3$ such as high PLQY with colloidal stability in non-polar solvents and narrow emission linewidth (22 nm) are highly suitable for LED applications. Therefore, prototype LEDs using purified nanoparticle samples of MA$_{0.87}$Cs$_{0.13}$PbBr$_3$ and CsPbBr$_3$ were fabricated. The LED structure is comprised of indium tin oxide (ITO)/poly(3,4-ethylenedioxythiophene) polystyrene sulfonate (PEDOT:PSS, 45 nm)/poly(4-butylphenyl-diphenylamine) (poly-TPD, 30 nm)/nanoparticles (20 nm)/2,4,6-tris[3-(diphenylphosphinyl)phenyl]-1,3,5-triazine (POT2T, 45 nm)/LiF (0.8 nm)/Al (100 nm) respectively (Fig. 3c). As presented in the energy diagram (Fig. 3c), PEDOT:PSS and poly-TPD act as the hole injecting layer, whereas POT2T serves as an electron injecting layer. The energy level data of the transport layers and CsPbBr$_3$ was reported earlier by Brown *et al.* illustrate (Fig. 3c) the compatibility of transport layers and photoactive CsPbBr$_3$ layer.[45] The inset of Fig. 3c shows a clear and stable colloidal solution and a photograph of LED at 4.0 V. As evident from JV curve, both LEDs exhibit low leakage current in the order of 10^{-4} mA cm^{-2} (Fig. 3d). However, the MA$_{0.87}$Cs$_{0.13}$PbBr$_3$ shows a low turn-on voltage of 2.0 V, whereas the CsPbBr$_3$ LED the turn-on voltage is 4.0 V. The LED electroluminescence (EL) spectra exhibit a slight red-shift compared to their original PL in suspension that is ascribed to the transition of nanoparticles from colloidal to thin-film form due to Förster resonance energy transfer

(FRET) between neighbouring nanoparticles (Fig. 3e).[46] Fig. 1e, S2 and Table S2† show the current efficiency, power efficiency, and EQE *vs.* current density curve of both LEDs; the MA$_{0.87}$Cs$_{0.13}$PbBr$_3$ LED shows a current efficiency of 2.8 cd A^{-1} with EQE of 0.83% and power efficiency of 2.34 lm W^{-1}, whereas, the CsPbBr$_3$ LED only exhibits a current efficiency of 0.64 cd A^{-1} with EQE of 0.20% and power efficiency of 0.41% lm W^{-1}. Future work will likely improve the performance of these LED prototypes. While the efficiency values in both devices are low, the MA$_{0.87}$Cs$_{0.13}$PbBr$_3$ LED shows a remarkable 4.3 times current efficiency compared to the standard CsPbBr$_3$ LEDs.

Conclusion

The development of Cs-MA mixed cation colloidal perovskites using a room-temperature LARP synthesis method has been investigated. Structural and compositional studies using powder XRD and XPS confirmed the incorporation of Cs$^+$ on the "A" site of MAPbBr$_3$ nanoparticles with high PLQY achieved ranging from 60–88%. TRPL demonstrated increased charge carrier lifetime for optimized MA$_{0.87}$Cs$_{0.13}$PbBr$_3$ which in turn results in a PLQY of ~88%. The increment in PLQY for mixed-cation nanoparticles was attributed to the relaxation in structural strain. However, investigation at the atomic scale is needed to establish the origin of local strain in these hybrid perovskites. Lastly, the colloidally stable ink of 13 mol% Cs and CsPbBr$_3$ were used to fabricate into functioning electrically-driven LED prototypes.
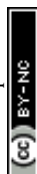
Conflicts of interest

There are no conflicts to declare.

Acknowledgements

References

1 *Best Research Cell Efficiency*, https://www.nrel.gov/pv/assets/pdfs/pv-efficiency-chart.201812171.pdf, 2019.

2 B. Zhao, S. Bai, V. Kim, R. Lamboll, R. Shivanna, F. Auras, J. M. Richter, L. Yang, L. Dai, M. Alsari, X.-J. She, L. Liang, J. Zhang, S. Lilliu, P. Gao, H. J. Snaith, J. Wang, N. C. Greenham, R. H. Friend and D. Di, *High-efficiency perovskite–polymer bulk heterostructure light-emitting diodes*, 2018.

3 P. Vashishtha, M. Ng, S. B. Shivarudraiah and J. E. Halpert, *Chem. Mater.*, 2018, **31**, 83–89.

4 L. Xie, P. Vashishtha, T. M. Koh, P. C. Harikesh, N. F. Jamaludin, A. Bruno, T. J. Hooper, J. Li, Y. F. Ng and S. G. Mhaisalkar, *Adv. Mater.*, 2020, **32**, 2003296.

5 Y. Dong, Y.-K. Wang, F. Yuan, A. Johnston, Y. Liu, D. Ma, M.-J. Choi, B. Chen, M. Chekini and S.-W. Baek, *Nat. Nanotechnol.*, 2020, **15**, 668–674.

6 M. Jeong, I. W. Choi, E. M. Go, Y. Cho, M. Kim, B. Lee, S. Jeong, Y. Jo, H. W. Choi and J. Lee, *Science*, 2020, **369**, 1615–1620.

7 R. R. Tamming, J. Butkus, M. B. Price, P. Vashishtha, S. K. K. Prasad, J. E. Halpert, K. Chen and J. M. Hodgkiss, *ACS Photonics*, 2019, **6**, 345–350.

8 M. M. Lee, J. Teuscher, T. Miyasaka, T. N. Murakami and H. J. Snaith, *Science*, 2012, **338**, 643–647.

9 S. D. Stranks and H. J. Snaith, *Nat. Nanotechnol.*, 2015, **10**, 391–402.

10 V. Kumar, J. Barbé, W. L. Schmidt, K. Tsevas, B. Ozkan, C. M. Handley, C. L. Freeman, D. C. Sinclair, I. M. Reaney and W. C. Tsoi, *J. Mater. Chem. A*, 2018, **6**, 23578–23586.

11 B. Slimi, M. Mollar, I. Ben Assaker, A. Kriaa, R. Chtourou and B. Mari, *Monatshefte für Chemie*, 2017, **148**, 835–844.

12 P. Vashishtha, S. Bishnoi, C.-H. Angus Li, M. Jagadeeswararao, T. J. N. Hooper, N. Lohia, S. B. Shivarudraiah, M. S. Ansari, S. N. Sharma and J. E. Halpert, *ACS Appl. Electron. Mater.*, 2020, **2**(11), 3470–3490.

13 P. Vashishtha, S. A. Veldhuis, S. S. Dintakurti, N. L. Kelly, B. E. Griffith, A. A. Brown, M. S. Ansari, A. Bruno, N. Mathews and Y. Fang, *J. Mater. Chem. C*, 2020, **8**, 11805–11821.

14 M. Saliba, T. Matsui, J.-Y. Seo, K. Domanski, J.-P. Correa-Baena, M. K. Nazeeruddin, S. M. Zakeeruddin, W. Tress, A. Abate and A. Hagfeldt, *Energy Environ. Sci.*, 2016, **9**, 1989–1997.

15 H. P. Kim, J. Kim, B. S. Kim, H. M. Kim, J. Kim, A. R. b. M. Yusoff, J. Jang and M. K. Nazeeruddin, *Adv. Opt. Mater.*, 2017, **5**, 1600920.

16 G. Kim, H. Min, K. S. Lee, D. Y. Lee, S. M. Yoon and S. I. Seok, *Science*, 2020, **370**, 108.

17 X. Li, Y. Luo, M. V. Holt, Z. Cai and D. P. Fenning, *Chem. Mater.*, 2019, **31**, 2778–2785.

18 L. Zhang, X. Yang, Q. Jiang, P. Wang, Z. Yin, X. Zhang, H. Tan, Y. M. Yang, M. Wei and B. R. Sutherland, *Nat. Commun.*, 2017, **8**, 15640.

19 M. I. Saidaminov, J. Kim, A. Jain, R. Quintero-Bermudez, H. Tan, G. Long, F. Tan, A. Johnston, Y. Zhao, O. Voznyy and E. H. Sargent, *Nat. Energy*, 2018, **3**, 648–654.

20 X. Zhang, H. Liu, W. Wang, J. Zhang, B. Xu, K. L. Karen, Y. Zheng, S. Liu, S. Chen and K. Wang, *Adv. Mater.*, 2017, **29**, 1606405.

21 C. Zhang, S. Wang, X. Li, M. Yuan, L. Turyanska and X. Yang, *Adv. Funct. Mater.*, 2020, 1910582.

22 X. Dai, Z. Zhang, Y. Jin, Y. Niu, H. Cao, X. Liang, L. Chen, J. Wang and X. Peng, *Nature*, 2014, **515**, 96–99.

23 P. O. Anikeeva, J. E. Halpert, M. G. Bawendi and V. Bulovic, *Nano Lett.*, 2009, **9**, 2532–2536.

24 J. Song, J. Li, L. Xu, J. Li, F. Zhang, B. Han, Q. Shan and H. Zeng, *Adv. Mater.*, 2018, **30**, 1800764.

25 S. Premkumar, K. Kundu and S. Umapathy, *Nanoscale*, 2019, **11**, 10292–10305.

26 C. J. Bartel, C. Sutton, B. R. Goldsmith, R. Ouyang, C. B. Musgrave, L. M. Ghiringhelli and M. Scheffler, *Sci. Adv.*, 2019, **5**, eaav0693.

27 J. Butkus, P. Vashishtha, K. Chen, J. K. Gallaher, S. K. Prasad, D. Z. Metin, G. Laufersky, N. Gaston, J. E. Halpert and J. M. Hodgkiss, *Chem. Mater.*, 2017, **29**, 3644–3652.

28 S. A. Veldhuis, Y. F. Ng, R. Ahmad, A. Bruno, N. F. Jamaludin, B. Damodaran, N. Mathews and S. G. Mhaisalkar, *ACS Energy Lett.*, 2018, **3**, 526–531.

29 S. Hirotsu, J. Harada, M. Iizumi and K. Gesi, *J. Phys. Soc. Jpn.*, 1974, **37**, 1393–1398.

30 P. Cottingham and R. L. Brutchey, *Chem. Commun.*, 2016, **52**, 5246–5249.

31 C. Tenailleau, S. Aharon, B.-E. Cohen and L. Etgar, *Nanoscale Adv.*, 2019, **1**, 147–153.

32 F. Weigert, A. Müller, I. Häusler, D. Geißler, D. Skroblin, M. Krumrey, W. Unger, J. Radnik and U. Resch-Genger, *Sci. Rep.*, 2020, **10**, 1–15.

33 C. Ferraris, M. Srinivasan and T. J. White, *Acta Crystallogr., Sect. A: Found. Crystallogr.*, 2008, **64**, C536–C537.

34 M. R. Linaburg, E. T. McClure, J. D. Majher and P. M. Woodward, *Chem. Mater.*, 2017, **29**, 3507–3514.

35 U. Holzwarth and N. Gibson, *Nat. Nanotechnol.*, 2011, **6**, 534.

36 J. Huang, Y.-H. Wu, Z.-G. Zhu, W. Y. Shih and W.-H. Shih, *Chem. Phys. Lett.*, 2018, **702**, 21–25.

37 T. Yin, Y. Fang, X. Fan, B. Zhang, J.-L. Kuo, T. J. White, G. M. Chow, J. Yan and Z. X. Shen, *Chem. Mater.*, 2017, **29**, 5974–5981.

38 X. Y. Chin, A. Perumal, A. Bruno, N. Yantara, S. A. Veldhuis, L. Martínez-Sarti, B. Chandran, V. Chirvony, A. S.-Z. Lo and J. So, *Energy Environ. Sci.*, 2018, **11**, 1770–1778.

39 S. Bhaumik, S. A. Veldhuis, Y. F. Ng, M. Li, S. K. Muduli, T. C. Sum, B. Damodaran, S. Mhaisalkar and N. Mathews, *Chem. Commun.*, 2016, **52**, 7118–7121.

40 P. Vashishtha, B. E. Griffith, A. A. M. Brown, T. J. N. Hooper, Y. Fang, M. S. Ansari, A. Bruno, S. H. Pu, S. G. Mhaisalkar, T. White and J. V. Hanna, *ACS Appl. Electron. Mater.*, 2020, **2**, 4002–4011.

41 S. Zhou, R. Tang, H. Li, L. Fu, B. Li and L. Yin, *J. Power Sources*, 2019, **439**, 227065.

42 Y. Chen, Y. Lei, Y. Li, Y. Yu, J. Cai, M.-H. Chiu, R. Rao, Y. Gu, C. Wang, W. Choi, H. Hu, C. Wang, Y. Li, J. Song, J. Zhang, B. Qi, M. Lin, Z. Zhang, A. E. Islam, B. Maruyama,
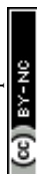
S. Dayeh, L.-J. Li, K. Yang, Y.-H. Lo and S. Xu, *Nature*, 2020, **577**, 209–215.

43 L. Leppert, S. E. Reyes-Lillo and J. B. Neaton, *J. Phys. Chem. Lett.*, 2016, **7**, 3683–3689.

44 J. Shi, F. Li, J. Yuan, X. Ling, S. Zhou, Y. Qian and W. Ma, *J. Mater. Chem. A*, 2019, **7**, 20936–20944.

45 A. A. M. Brown, T. J. N. Hooper, S. A. Veldhuis, X. Y. Chin, A. Bruno, P. Vashishtha, J. N. Tey, L. Jiang, B. Damodaran and S. H. Pu, *Nanoscale*, 2019, **11**, 12370–12380.

46 P. Vashishtha and J. E. Halpert, *Chem. Mater.*, 2017, **29**, 5965–5973.